Climate Dynamics (2023) 61:2457–2470
https://doi.org/10.1007/s00382-023-06693-y

Energetic connection between the South China Sea summer monsoon and Indian Ocean dipole from the perspective of perturbation potential energy

Yazhou Zhang[1,2] · Jianping Li[1,3] · Yina Diao[1] · Zhaolu Hou[1] · Ting Liu[2,4] · Bin Zuo[5]

Received: 1 December 2022 / Accepted: 31 January 2023 / Published online: 7 February 2023

Abstract

This study investigates the role of perturbation potential energy (PPE) in energetic connection between the South China Sea summer monsoon (SCSSM) and Indian Ocean dipole (IOD). When the SCSSM is strong during boreal summer, the higher and lower PPE anomalies controlled primarily by the diabatic heating correspond to negative and positive energy conversion, favoring the ascending and descending motions over western North Pacific (WNP) and southern Maritime Continent (SMC), respectively. This implies the existence of the regional Hadley circulation. This regional Hadley circulation-induced lower southeasterly wind anomalies reduce the local sea surface temperature (SST) anomalies over the tropical southeastern Indian Ocean via the wind–evaporation–SST and wind–thermocline–SST feedbacks, increasing the zonal SST gradient over the tropical Indian Ocean. Thus, a positive IOD event develops in boreal summer, and verse vice. Although the SCSSM decays during boreal autumn, the increased gradient of the PPE anomalies intensifies the anomalous Walker circulation over the tropical Indian Ocean, providing positive feedback that allows the IOD to mature. Consequently, the PPE dipole over WNP and SMC serves as an energetic bridge between the SCSSM and IOD.

Keywords Energetic connection · South China Sea summer monsoon · Indian Ocean dipole · Perturbation potential energy

1 Introduction

The Indian Ocean dipole (IOD) is one of the most significant interannual variabilities over the tropical Indian Ocean and is characterized by the opposite variations in the sea surface temperature (SST) anomalies (Saji et al. 1999; Webster et al. 1999). The IOD has significant global climatic impacts (e.g., affecting East Africa, Maritime Continent, East Asia, South America, and Antarctica) that lead to the severe socioeconomic repercussions (Ashok et al. 2003; Guan and Yamagata 2003; Saji and Yamagata 2003; Cai et al. 2009; Ding et al. 2010; Nuncio and Yuan 2015; Chen et al. 2020; Zhou et al. 2021; Sena and Magnusdottir 2021). Therefore, improving our understanding of these impacts and the underlying physical processes associated with the IOD has important implications for the prevention and mitigation of these potential socioeconomic losses.

Previous studies have reported that the El Niño–Southern Oscillation (ENSO) is the dominant control on the IOD (Xie et al. 2002; Behera et al. 2006; Huang and Shukla 2007a; Schott et al. 2009; Yang et al. 2015; Zhang et al. 2015; Stuecker et al. 2017). However, some IOD events have also been observed in the absence of ENSO (Yamagata et al. 2003; Behera et al. 2006; Huang and Shukla 2007b; Yang et al. 2015; Zhang et al. 2018, 2019b). Using long-term simulations that excluded ENSO forcing, Huang and Shukla (2007b) indicated that these independent IOD events

✉ Jianping Li
ljp@ouc.edu.cn

✉ Yina Diao
diaoyn@ouc.edu.cn

1 Frontiers Science Center for Deep Ocean Multispheres and Earth System (FDOMES)/Key Laboratory of Physical Oceanography/Academy of the Future Ocean/College of Oceanic and Atmospheric Science, Ocean University of China, Qingdao, China

2 State Key Laboratory of Satellite Ocean Environment Dynamics, Second Institute of Oceanography, Ministry of Natural Resources, Hangzhou, China

3 Laoshan Laboratory, Qingdao, China

4 Southern Marine Science and Engineering Guangdong Laboratory (Zhuhai), Zhuhai, China

5 Dalian Naval Academy, Dalian, China

are closely associated with fluctuations in the northwestern Pacific monsoon. Zhang et al. (2018, 2021) used observations and the Coupled Model Intercomparison Project Phase 5 (CMIP5) models to demonstrate that the South China Sea summer monsoon (SCSSM) can significantly affect IOD growth via the regional Hadley circulation over the western North Pacific (WNP) and southern Maritime Continent (SMC) during the boreal summer (June–July–August, JJA).

The formation and maintenance of the atmospheric general circulation is essentially controlled by the kinetic energy of the climate system (Lorenz 1955); however, the diabatic heating cannot be converted directly into kinetic energy except through potential energy. Lorenz (1955) thus established the atmospheric available potential energy (APE) theory and indicated that the APE can act as a bridge between the diabatic heating and kinetic energy, although this is not appropriate at the regional scale because APE is calculated using the global mean. Based on this APE theory, Li and Gao (2006) proposed the concept of atmospheric perturbation potential energy (PPE), reflecting the maximum amount of total potential energy that can be converted into kinetic energy at the regional scale. The atmospheric PPE theory has been successfully applied to atmospheric energetics research into regional climate variability, such as the East Asia summer monsoon, SCSSM, IOD, and ENSO (Li et al. 2016; Dong et al. 2017; Huyan et al. 2017; Wang et al. 2019; Zhang et al. 2019a).

Zhang et al. (2018, 2019b, 2021) examined the dynamic connection between the SCSSM and IOD via the regional Hadley circulation using observations and CMIP5 models. Furthermore, Wang et al. (2019) and Zhang et al. (2019a) separately investigated atmospheric energetics processes and their relationship to circulation variations during IOD and SCSSM events using the PPE theory; however, the energetic connection between the SCSSM and IOD remains unclear. Consequently, this study focuses mainly on the atmospheric energetic connection between the SCSSM and IOD from the viewpoint of the PPE and provides a new prospective from which we might improve our understanding of the relationship between the SCSSM and IOD.

2 Theory and datasets

2.1 Atmospheric PPE theory

Margules (1910) first investigated the atmospheric energy availability in storms; subsequently, the modern framework for atmospheric energetics was established by Lorenz (1955), who proposed the APE theory. The APE theory promoted the development of the global atmospheric energy budget (Oort 1964, 1971; Peixóto and Oort 1974; Oort et al. 1989; Li et al. 2007, 2011; Kim and Kim 2013; Roullet et al. 2014; Pan et al. 2017; Kanno and Iwasaki 2022), but it was not a powerful tool for diagnosing regional energetics because it was calculated using the global average. Although several studies have tried to extend Lorenz's APE theory to the local scale by incorporating the boundary energy fluxes of the study region (Smith 1969; Johnson 1970; Smith et al. 1977; Edmon 1978), the original APE formulation was used in these studies. Moreover, the minimum total potential energy in the APE theory is defined as the atmospheric reference state of the APE under the conditions of horizontal and statically stable stratification (Lorenz 1955); however, this ideal reference condition is physically unrealistic because the atmospheric adiabatic redistribution is insufficiently physically constrained (Gao et al. 2006). Therefore, Gao et al. (2006) defined the conditional minimum reference state. On this basis, Li and Gao (2006) proposed the atmospheric PPE, which is defined as the difference between the total potential energy and the conditional minimum reference state via any adiabatic redistribution. The PPE equation can be expressed as follows, using isobaric coordinates (complete derivations can be found in Li and Gao 2006):

$$\mathrm{PPE}=\sum_{i=1}^{\infty}\mathrm{PPE}_i=\sum_{i=1}^{\infty}\frac{p_{00}^{(i-1)\kappa}\prod_{j=01}^{i=1}(1+\kappa-j)}{i!\gamma_d(1+\kappa)}\int_0^{p_s}\frac{T'^i}{P^{(i-1)(1+\kappa)}}\left(-\frac{\partial\bar{\theta}}{\partial p}\right)^{-i+1}dp, \tag{1}$$

where i is the order of the moment term of PPE; p, p_{00}, and p_s are the pressure, reference pressure (generally 1000 hPa), and surface pressure, respectively; R(287 J kg^{-1} K^{-1}) is the gas constant of dry air; c_p (1004 J kg^{-1} K^{-1}) is the specific heat at a constant pressure; $\kappa = R/c_p$; $\gamma_d = g/c_p$ is the dry adiabatic lapse rate, where g (9.80665 m s^{-2}) is the acceleration due to gravity; $\bar{\theta}$ (K) is the potential temperature at the reference state; and T' (K) is the departure of the air temperature. Thus, the mathematical expressions of the first and second moment terms of PPE can be written as follows:

$$\mathrm{PPE}_1=\frac{1}{\gamma_d}\int_0^{P_S}T'dp, \tag{2}$$

$$\mathrm{PPE}_2=\frac{\kappa p_{00}^{\kappa}}{2\gamma_d}\int_0^{P_S}\frac{T'^2}{p^{1+\kappa}}\left(-\frac{\partial\bar{\theta}}{\partial p}\right)^{-1}dp, \tag{3}$$

where PPE_1 and PPE_2 denote the first and second moment terms of PPE, respectively. In contrast to the higher-moment terms of PPE, PPE_1 and PPE_2 are the dominant terms at the local scale (Li and Gao 2006). Thus, in this study, atmospheric PPE is defined as the sum of PPE_1 and PPE_2.

2.2 Datasets and indices

The monthly mean atmospheric circulation variables used were as follows: air temperature, zonal wind, meridional wind, vertical velocity through the whole troposphere

(1000–300 hPa), sea level pressure, precipitation rate, precipitable water content, and surface heat fluxes (i.e., sensible heat, latent heat, shortwave radiation, and longwave radiation fluxes). These variables, with a horizontal gridded resolution of 2.5° × 2.5°, were obtained from the National Centers for Environmental Prediction–National Center for Atmospheric Research (NCEP/NCAR) reanalysis dataset for the period 1948–2020 (Kalnay et al. 1996). The improved Extended Reconstructed SST version 5 (ERSST v5) dataset on a 2° × 2° grid and covering the same period is used (Huang et al. 2017). We used sea surface height (SSH) as a proxy for thermocline variability during between 1948–2010 (Yu 2003), which is obtained from the Simple Ocean Data Assimilation (SODA, version 2.2.4) reanalysis dataset on a 0.5° × 0.5°grid (Carton and Giese 2008). The linear trend and the long-term (1948–2010) mean climatology were removed from each dataset prior to analysis.

The dynamical normalized seasonality monsoon index defined by Li and Zeng (2002, 2003) captures well the seasonal cycle and interannual variability of the seasonal wind field in global monsoon regions (Li et al. 2010; Huyan et al. 2017; Liu et al. 2018; Zhang et al. 2018, 2019b, 2021). This index is defined as follows:

$$\delta = \frac{\left\|\overline{\mathrm{V}}_1 - \mathrm{V}_{m,n}\right\|}{\left\|\overline{\mathrm{V}}\right\|} - 2$$

where ||*|| denote a norm on the monsoon domain of integration. $\overline{\mathrm{V}}_1$ and $\overline{V}$ are the climatological mean wind vectors in January and the mean of the January and July climatological wind vectors, respectively. $V_{m,n}$ denotes the monthly wind vectors in the mth month of the nth year. The SCSSM index (SCSSMI) is calculated as the area-average over the South China Sea monsoon domain (100°–125 °E, 0°–25 °N) at 925 hPa wind field during JJA using the dynamical normalized seasonality (available at http://lijianping.cn/dct/page/65578). In addition, the IOD mode index (DMI) is defined as the difference in SST anomalies between the tropical western (50°–70°E, 10°S–10°N) and southeastern (90°–110 °E, 10° S–0°) Indian Ocean. We used the Niño 3.4 area-averaged SST anomalies over the equatorial central Pacific Ocean (120° W–170° W, 5° S–5° N) to monitor ENSO.

2.3 Methods

The correlation and regression analyses were used to evaluate the PPE variations in processes of the SCSSM affecting the IOD. We used partial correlation analysis to examine the potential influence of ENSO. The significance of correlations between our chosen pair of indices, X and Y, can be tested using a two-tailed Student's t test, in which the effective number of degrees of freedom (N_{eff}) is calculated using the following approximation (e.g., Bretherton et al. 1999; Li et al. 2013):

$$\frac{1}{N_{eff}} \approx \frac{1}{N} + \frac{2}{N}\sum_{i=1}^{N}\frac{N-i}{N}\rho_{XX}(i)\rho_{YY}(i),$$

where N is the total sample size, and $\rho_{XX}(i)$ and $\rho_{YY}(i)$ are the autocorrelations of the time series X and Y, respectively, at time lag i.

3 Energetic relationship between the SCSSM and IOD

The correlation between the SCSSM and JJA IOD is significant and has a value of 0.5, and this correlation increases to 0.62 during the boreal autumn (September–October–November [SON]; Fig. 1a). Compared with the western pole of the IOD, the SCSSM has a significant correlation coefficient (−0.5) with the eastern pole of JJA IOD (Fig. 1a). This situation intensifies during SON (−0.58), although the correlation between the SCSSM and the western pole of the IOD during SON also becomes significant (0.42; Fig. 1a). These results imply that there is an intimate relationship between the SCSSM and the IOD, especially for the eastern pole of the IOD. The significant positive precipitation anomalies associated with the SCSSM are clearly observed over the WNP, together with the negative precipitation anomalies over the SMC, forming a remarkable precipitation dipole pattern (Fig. 1b). This precipitation dipole corresponds the regional Hadley circulation over the WNP and SMC, which acts as an atmospheric bridge between the SCSSM and the IOD (Zhang et al. 2018, 2019b, 2021), whereas the circulation is essentially controlled by energy variation.

To further explore the energetic connection between the SCSSM and IOD, Fig. 1c shows the regression of the PPE anomalies onto the SCSSMI during JJA. A remarkable PPE dipole (PPED) pattern associated with the SCSSM is clearly observed over the WNP and SMC. We further defined the PPED index as the difference in PPE anomalies between the WNP and SMC. The high correlation coefficients indicate the close connections between the PPED and SCSSM (0.71) and also between the PPED and IOD (0.45). These preliminary results suggest that the PPED may act as the energy bridge that links the SCSSM and IOD.

We also used partial correlation analysis to validate the above results. After removal of the PPED signals, the correlation between the SCSSM and IOD became 0.29 (Table 1). Although this is still significant, the explained variance was reduced by ~ 17%, illustrating the key role of the PPED as a bridge between the SCSSM and IOD.

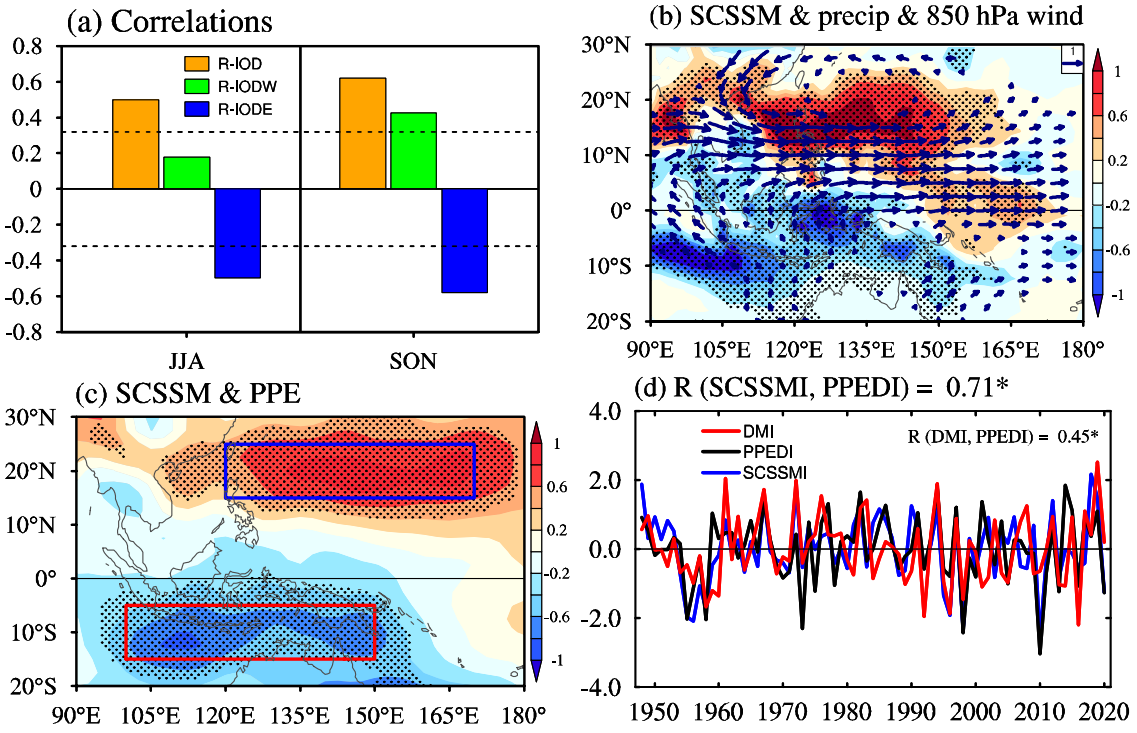

Fig. 1 **a** Correlations of the SCSSM with the IOD (R-IOD, orange bars), western pole of the IOD (R-IODW, green bars), and eastern pole of the IOD (R-IODE, blue bars) during JJA and SON. **b** Regressions of the precipitation (mm day^{-1}) and 850 hPa wind (m s^{-1}) anomalies onto the SCSSMI during JJA. **c** as **b**, but for the PPE (10^6 J m^{-2}) anomalies. Black stipples in (**b**–**c**) indicate significance at the 90% level. Blue and red rectangles in **c** denote the western North Pacific (WNP, 120°–170° E, 15°–25° N) and the southern Maritime Continent (SMC, 100°–150° E, 15°–5° S) regions, respectively. **d** Standardized time series of the SCSSMI (blue line), DMI (red line), and PPEDI (black line) during JJA; *R* indicates that the correlation coefficient between the two series exceeds the 99% confidence level. Here, the PPE dipole index (PPEDI) is defined as the difference in atmospheric PPE anomalies between the WNP and SMC

Table 1 The partial correlation coefficients between the SCSSM and IOD during JJA (SON) for period of 1948–2020

	Correlations	Partial correlations		
		Rm-PPED	Rm-lower-level PPED	Rm-upper-level PPED
(SCSSMI, JJA DMI)	0.5**	0.29*	0.29*	0.46**
(SCSSMI, SON DMI)	0.62**	0.54**	0.56**	0.58**

Rm-PPED (lower-level PPED and upper-level PPED) indicates the removal of the JJA (SON) PPE dipole (lower-level PPED and upper-level PPED) signals. The one and two asterisks indicate 95% and 99% confidence level, respectively

4 Energy conversion and relevant atmospheric circulation variations

The energetic conversion between the atmospheric PPE and perturbation kinetic energy (PKE) is controlled by the following governing equations:

$$\frac{1}{g}\int_0^{P_S}\frac{\partial PPE}{\partial t}dp = \mathrm{C}_k+\mathrm{G}+\mathrm{HBF}_{PPE}, \tag{4}$$

$$\frac{1}{g}\int_0^{P_S}\frac{\partial PKE}{\partial t}dp = -\mathrm{C}_k+\ \mathrm{D}+\mathrm{HBF}_{PKE}, \tag{5}$$

$$\mathrm{C}_k = \frac{1}{g}\int_0^{P_S} w\alpha dp, \tag{6}$$

where C_k is the energy conversion term and depends on the vertical velocity (w) and air density (α). The capital letters G, D, and HBF denote the diabatic heating, viscous dissipation, and horizontal boundary fluxes, respectively. It is evident that the C_k is the only energy conversion term between the PPE and PKE. The negative (positive) C_k indicates that the PPE (PKE) is transformed into PKE (PPE).

The positive (negative) atmospheric PPE anomalies correspond to the negative (positive) C_k anomalies over the WNP (SMC) during the strong SCSSM years (Fig. 2), which

suggests that the PPE (PKE) anomalies can be converted into PKE (PPE) anomalies over the WNP (SMC). In Eq. (6), the C_k is directly associated with the atmospheric circulation changes. As cold air descends or warm air ascends, C_k is negative and energy is converted from PPE to PKE. Conversely, as cold air ascends or warm air descends, C_k is positive and energy is converted from PKE to PPE.

The vertical–meridional distribution of the C_k and circulation related to the SCSSM averaged between 100°E and 170°E is shown in Fig. 3a and further supports the above results. Significant negative C_k anomalies are located at roughly 15°N (Fig. 3a), implying the existence of an anomalous upward branch of the regional Hadley circulation (Fig. 3b). Strong positive C_k anomalies are centered at 10° S, accompanied by an anomalous downward motion between 30°S and 0° (Fig. 3a, b). This suggests the existence of an anomalous regional Hadley circulation over the WNP and SMC (Fig. 3b), which agrees with the results of Zhang et al. (2018, 2019b, 2021).

As the PPE transformation occurs at different atmospheric levels (Wang et al. 2012), Fig. 3c shows the regressions of the vertical–meridional PPE anomalies averaged between 100° E and 170° E on the SCSSMI during JJA. The positive PPE anomalies related to the SCSSM over WNP are significant through the whole troposphere (1000–300 hPa), but especially at upper levels (600–300 hPa; Fig. 3c). In contrast, the significant negative PPE anomalies are clearly observed in the lower troposphere (1000–700 hPa) over SMC, together with the weakly positive PPE anomalies in the upper troposphere (600–300 hPa; Fig. 3c).

A similar pattern can also be seen in the spatial distribution of the PPE anomalies in the lower and upper troposphere during JJA. The prominent PPED is clearly evident over the WNP and SMC through the whole troposphere (1000–300 hPa; Fig. 4a); meanwhile, there is an obvious PPE dipole pattern over the tropical Indian Ocean, albeit with a weaker intensity over the tropical western Indian Ocean (Figs. 3d, 4a). In fact, the significant PPE anomalies over the WNP occur mainly in the upper troposphere (600–300 hPa), whereas the lower troposphere (1000–700 hPa) PPE anomalies are significant over SMC and the tropical western Indian Ocean (Figs. 3d, 4b–c). Thereby, the anomalous PPE dipole pattern over the tropical Indian Ocean is significant only in the lower troposphere (1000–700 hPa).

The PPE variations associated with the SCSSM occur mainly over SMC during JJA, leading to the weak zonal gradient of the PPE anomalies over the tropical Indian Ocean (Fig. 3d). The positive C_k anomalies are thus observed over SMC only during JJA (Fig. 3e), and this corresponds to the prominent downward motion over SMC at that time (Fig. 3f), reinforcing the local surface southeasterly wind anomalies (Fig. 1b). On the one hand, this enhanced surface southeasterly wind anomalies shift to be the southwesterly wind after crossing the equator, further promoting the development of SCSSM when superimposed on the JJA-mean southwesterly wind. This implies that the SCSSM can maintain self-development through the positive convection–PPE–circulation feedback. On the other hand, the enhanced surface southeasterly wind anomalies favor an increase in the local SST via the wind–evaporation–SST (WES) and wind–thermocline–SST (Bjerknes) feedbacks (Figs. 1b and 5a–c; Zhang et al. 2018, 2019b, 2021). With the increase in the zonal gradient of the SST anomalies over the tropical Indian Ocean, the positive IOD events begin to grow during JJA (Fig. 5c). Although the cloud–radiation–SST feedback plays a damping role in the IOD growth, the resultant contributions are much weaker than that associated with the Bjerknes and WES feedbacks. This further demonstrates that the processes of the SCSSM affecting the IOD are primarily controlled by the positive Bjerknes and WES feedbacks.

As the SCSSM decays during SON, the positive PPE anomalies over the WNP become negative anomalies

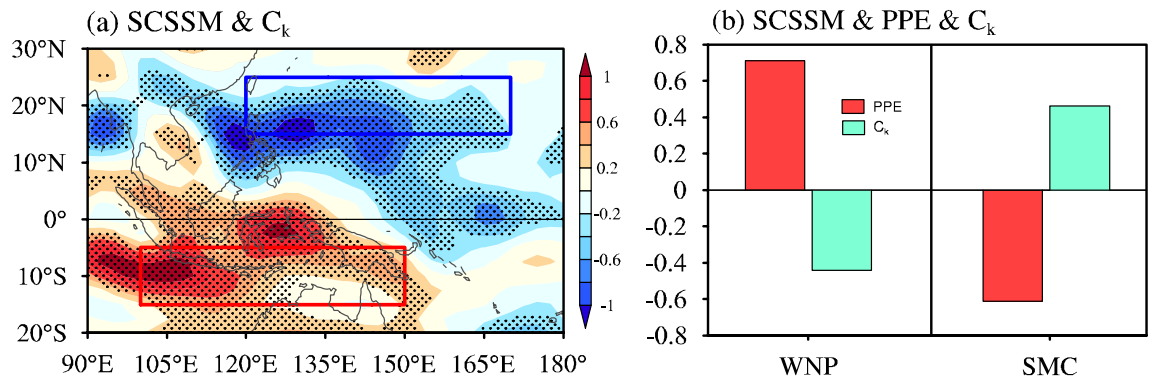

Fig. 2 **a** Regressions of atmospheric energy coversion term (C_k, 10^2 W m^{-2}) anomalies onto the SCSSMI during JJA. Blue and red rectangles denote the WNP and SMC regions as in Fig. 1b, respectively. **b** The area-averaged regression coefficients of the PPE (red bars, 10^6 J m^{-2}) and C_k (green bars, 10^2 W m^{-2}) on the SCSSMI over the WMP and SMC in **a**. Black stipples in **a** indicate that the values are significant at the 90% confidence level

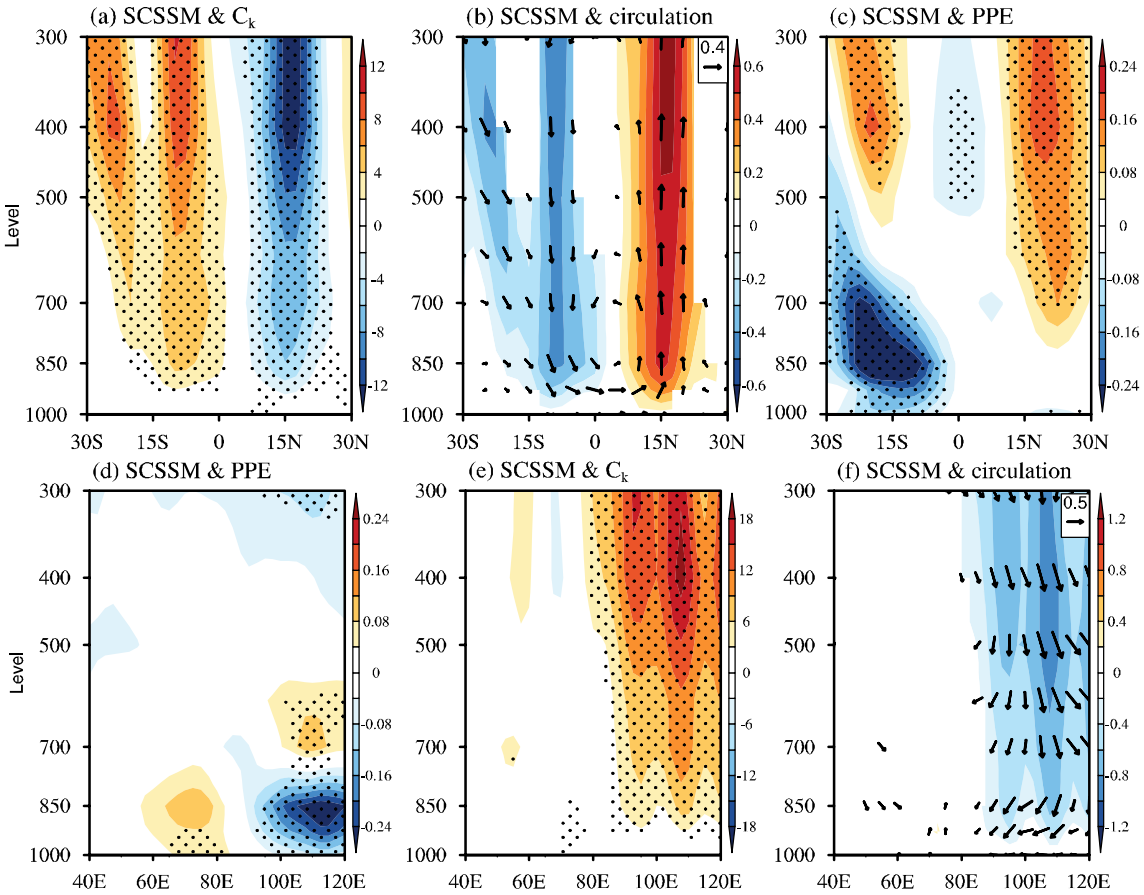

Fig. 3 Regressions of the meridional-vertical **a** C_k (W m^{-2}), **b** circulation (vectors, m s^{-1}) and vertical pressure velocity (shading, -10^{-2} Pa s^{-1}), and **c** PPE anomalies (10^6 J m^{-2}) onto the SCSSMI during JJA averaged between 100° E and 170° E. **d**–**f** as **a**–**c**, but for zonal-vertical (**d**) PPE anomalies (10^6 J m^{-2}), **e** C_k (W m^{-2}), and **f** circulation (vectors, m s^{-1}) and vertical pressure velocity anomalies (shading, -10^{-2} Pa s^{-1}) averaged between 0° and 10°S during JJA. Black stipples in **a**, **c**, **d**, **e** and shading and vectors in **b**, **f** indicate the 90% confidence level

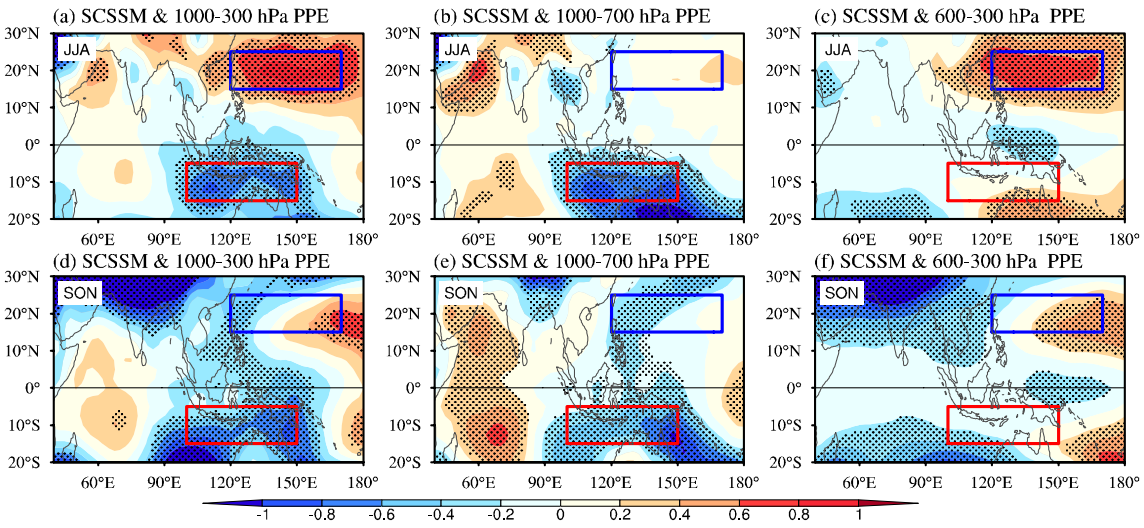

Fig. 4 Regressions of the PPE (10^6 J m^{-2}) anomalies in the **a** whole troposphere (1000–300 hPa), **b** lower troposphere (1000–700 hPa), and **c** upper troposphere (600–300 hPa) onto the SCSSMI during JJA. **d**–**f** as **a**–**c**, but for SON. Black stipples in **a**–**f** indicate that the values are significant at the 90% confidence level

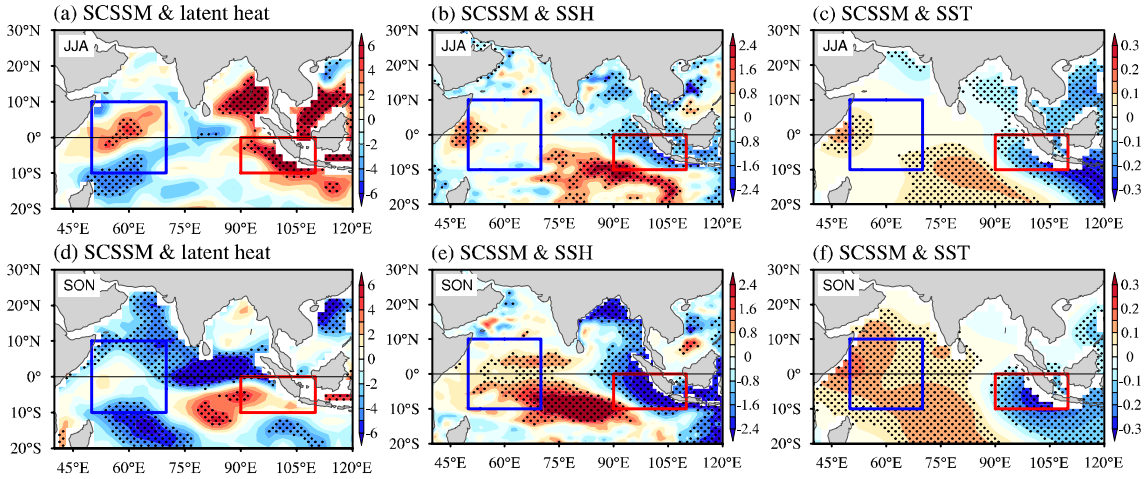

Fig. 5 Regressions of **a** the surface latent heat (W m^{-2}), **b** sea surface height (SSH, 10^{-2} m), and **c** SST (°C) anomalies onto the SCSSMI during JJA. **d–f**) as **a–c**, but for SON. Black stipples in **a–f** indicate that the values are significant at the 90% confidence level

through the whole troposphere (1000–300 hPa), while the PPE dipole over the tropical Indian Ocean further intensifies (Figs. 4d, 6a). This marked PPE dipole over the tropical Indian Ocean is more significant in the lower troposphere (1000–700 hPa), whereas the upper troposphere (600–300 hPa) PPE anomalies are uniformly weak (Figs. 4e–f, 6a). These results are consistent with Wang et al. (2019), who found that the lower-level (1000–850 hPa) PPE anomalies are the dominant layer of the PPE through the whole troposphere during the IOD events. The gradient of the PPE anomalies increases markedly over the tropical Indian Ocean (Fig. 6a). Significant negative C_k anomalies occur over the tropical southeastern Indian Ocean, together with the tropical western Indian Ocean, suggesting intensification of the Walker circulation (Figs. 6b–c). This enhanced Walker circulation provides a positive wind–thermocline–SST (Bjerknes) feedback that assists the maturation of the IOD events during SON (Figs. 5d–f). These results indicate that the lower troposphere (1000–700 hPa) PPE anomalies over the tropical Indian Ocean may play a major role in the development of the IOD events.

Therefore, we further defined the lower (1000–700 hPa) and upper (600–300 hPa) tropospheric PPED. After removing the lower-troposphere PPED signals, the correlation between the SCSSM and the JJA IOD decreased from 0.5 to 0.29 (Table 1), and although it remained significant at the 95% confidence level, the explained variance was reduced by ~ 17%. This correlation was also slightly weakened, to a value of 0.46, after removal of the upper tropospheric PPED signals (Table 1). The PPED disappears with the decay of

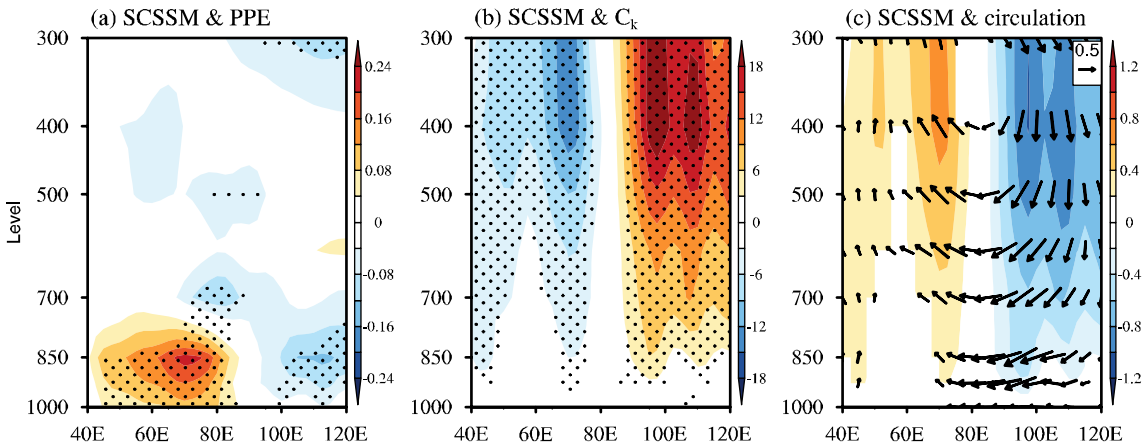

Fig. 6 Regressions of the zonal-vertical **a** PPE anomalies (10^6 J m^{-2}), **b** C_k (W m^{-2}), and **c** circulation (vector, m s^{-1}) and vertical pressure velocity anomalies (shading, -10^{-2} Pa s^{-1}) averaged between 0° and 10° S onto the SCSSMI during SON. Black stipples in **a**, **b** and shading and vectors in **c** indicate the 90% confidence level

the SCSSM in SON; thus, the correlations between the SCSSM and SON IOD change barely after excluding the PPED signals in SON (Table 1). These relationships further highlight the close link between the SCSSM and upper-tropospheric PPE anomalies over WNP and between the IOD and lower-tropospheric PPE anomalies over SMC in JJA. Overall, the PPE dipole over WNP and SMC serves as the key bridge that links the SCSSM to IOD in JJA.

In addition, both the SCSSM and IOD are closely associated with the ENSO (Wang et al. 2009; Zhang et al. 2019b). It is necessary to examine the possible influence of the ENSO. The aforementioned results indicate that the SCSSM can affect the IOD in JJA through the PPED over the WNP and SMC. Excluding the ENSO signals from the boreal preceding winter (Pre-DJF) to simultaneous JJA, the correlations between the SCSSM and PPED still exceed 0.7, which is significant at 99% confidence level (Table 2). Similar results can be found in the relationship between the SCSSM and IOD during JJA and SON (Table 2). These results demonstrate that the ENSO has little influence on the relationship or energy processes between the SCSSM and IOD.

5 Diabatic heating to atmospheric PPE

Atmospheric diabatic heating cannot lead directly to changes in PKE that drive the atmospheric general circulation (Lorenz 1955), but must first change PPE according to the governing Eqs. (4) and (5). This suggests that the atmospheric PPE acts as a link between diabatic heating and atmospheric circulation. Thus, it is necessary to diagnose the terms that contribute to the variations in PPE. On the basis of Eq. (4), the variations in PPE are determined mainly by the diabatic heating (G), C_k, and the horizontal boundary flux (HBF). Compared with the C_k and horizontal boundary flux (HBF), the diabatic heating (G) that links to the external forcing is the major contributor to the PPE variations (Dong et al. 2017; Huyan et al. 2017; Zhang et al. 2019a). Therefore, we examine the effects of diabatic heating (G) on PPE variations.

The diabatic heating (G) generally comprises the fluxes in surface sensible heat, latent heat, shortwave radiation, and longwave radiation. Similar but opposite dipole patterns in the surface latent heat, sensible heat, and longwave radiation fluxes related to the SCSSM occur over the WNP and the SMC (Figs. S7a–c), implying that these three surface heat fluxes are not conducive to the increase (decrease) in PPE anomalies over WNP (SMC). Although the shortwave radiation flux anomalies favor the PPE variations over WNP and SMC (Fig. 7d), the combined effects of all surface heat fluxes make little contribution to PPE over the WNP and even inhibit PPE over SMC (Fig. 7e–f). Overall, the surface heat fluxes may not be the major contributor to the PPE anomalies over WNP and SMC.

In addition to the surface heat fluxes, the latent heating released by condensation is also an important component of the diabatic heating (G), which can be generally measured using the precipitable water content (Huyan et al. 2017). Both the spatial location and pattern of the precipitable water content agree well with the PPE anomalies over WNP and SMC (Fig. 8a), which indicates the important role of latent heat release in generating the PPE variations. Furthermore, the change of the PPE lags the precipitation variation induced by SCSSM over the WNP by about 2 weeks, implying the influence of the precipitation on the PPE over the WNP (Zhang et al. 2019a). To further quantify the contribution of the latent heat release to the PPE, we also calculated the apparent heat source (Q_1) and apparent moisture sink (Q_2) using the equations developed in previous studies (Yanai and Tomita 1998; Hsu and Li 2011; Zhang et al. 2019a):

$$\langle Q_1 \rangle = c_p \frac{\partial T}{\partial t} - c_p(\omega\sigma - \mathrm{V} \cdot \nabla T), \tag{7}$$

$$\langle Q_2 \rangle = -L\left(\frac{\partial q}{\partial t} + \mathrm{V} \cdot \nabla q + \omega \frac{\partial q}{\partial p}\right), \tag{8}$$

where $\sigma = (RT/c_p p) - (\partial T/\partial p)$ is the static stability, V is the horizontal velocity, ∇ is the isobaric gradient operator, L is the latent heat of condensation, and q is the specific humidity. $\langle Q_* \rangle$ denotes the integration from 300 hPa to the surface and is expressed as follows:

Table 2 The partial correlation coefficients of the SCSSM with JJA IOD, SON IOD and JJA PPED after removing ENSO signals (Rm-ENSO) from the boreal preceding winter (Pre-DJF), spring (Pre-MAM) and simultaneous JJA

	Correlations	Partial correlations		
		Rm-ENSO Pre-DJF	Rm-ENSO MAM	Rm-ENSO JJA
(SCSSMI, JJA PPEDI)	0.71**	0.7**	0.71**	0.7**
(SCSSMI, JJA DMI)	0.5**	0.5**	0.51**	0.48**
(SCSSMI, SON DMI)	0.62**	0.62**	0.64**	0.6**

The one and two asterisks indicate 95% and 99% confidence level, respectively

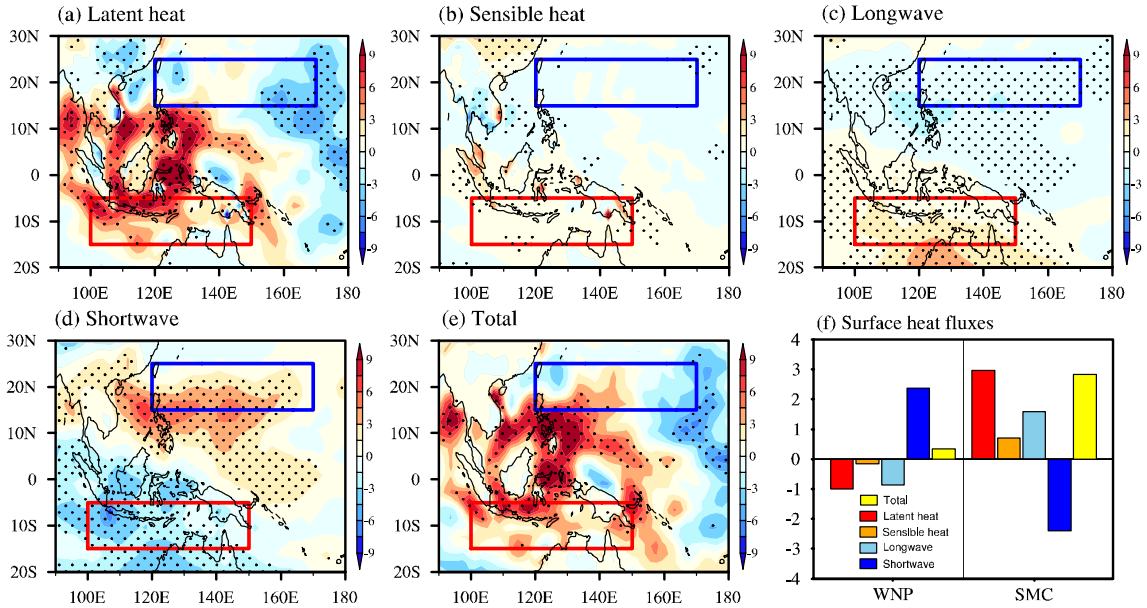

Fig. 7 Regressions of **a** the sensible heat (W m^{-2}), **b** latent heat (W m^{-2}), **c** longwave radiation (W m^{-2}), **d** shortwave radiation (W m^{-2}), and **e** total fluxes (W m^{-2}) anomalies onto the SCSSMI during JJA. **f** The area-averaged regression coefficients of the surface heat flux anomalies on the SCSSMI over the WNP and SMC regions in **a**–**e**. Black stipples in **a**–**e** indicate that the values are significant at the 90% confidence level

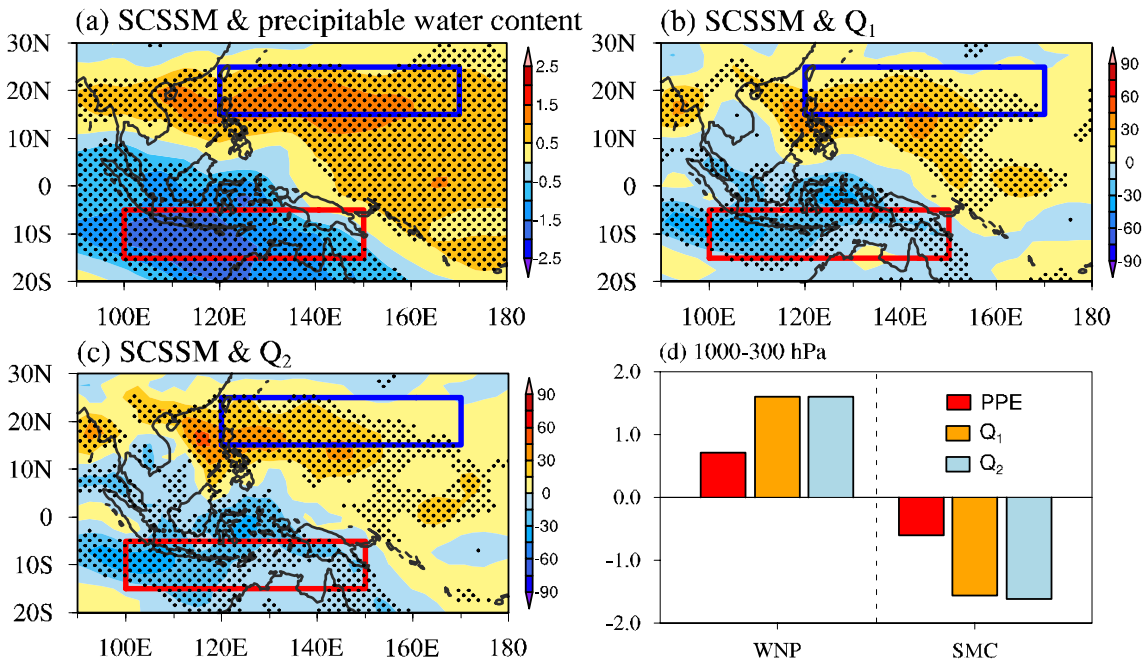

Fig. 8 Regressions of **a** the precipitable water content (kg m^{-2}), **b** Q_1 (W m^{-2}), and **c** Q_2 (W m^{-2}) anomalies onto the SCSSMI during JJA. **d** The area-averaged regression coefficients of the PPE (10^6 J m^{-2}), Q_1 (10 W m^{-2}), and Q_2 (10 W m^{-2}) anomalies on the SCSSMI over the WNP and SMC regions. Black stipples in **a**–**c** indicate that the values are significant at the 90% confidence level

$$\langle Q_* \rangle = \frac{1}{g} \int_{300}^{P_{00}} Q_* dp. \tag{9}$$

Resembling the PPE and precipitable water content anomalies (Figs. 1b, 8a), both the Q_1 and Q_2 anomalies exhibit a prominent dipole pattern over the WNP and SMC (Fig. 8b and c), which assists the enhancement of the local

PPE anomalies. The similar magnitude of Q_1 and Q_2 over the WNP and SMC indicate that the latent heat released by condensation is the major contributor to the PPE anomalies (Fig. 8d).

The distinctly different vertical PPE variations over WNP and SMC are closely associated with the vertical distribution of diabatic heating. The magnitude of the Q_1 anomalies is much larger in the upper troposphere (600–300 hPa) than in the lower troposphere (1000–700 hPa) over WNP and SMC (Fig. 9a). Compared with Q_1, the extremum centers of the Q_2 anomalies associated with the SCSSM control the lower troposphere over both the WNP and SMC (Fig. 9b). These results imply that Q_1 and Q_2 make different contributions to the PPE anomalies at different levels in the troposphere. Our quantitative results are shown in Figs. 9c–d. In the lower troposphere (1000–700 hPa), both the Q_1 and Q_2 anomalies are larger over the WNP than that over the SMC, leading to the locally stronger (weaker) PPE anomalies over the WNP (SMC; Fig. 9c). Moreover, the Q_2 anomalies are more than $2\times$ greater than the Q_1 anomalies over both the WNP and SMC (Fig. 9c), which suggests that Q_2 is the major cause of the PPE variations in the lower troposphere (1000–700 hPa).

In contrast, the Q_1 anomalies in the upper troposphere (600–300 hPa) are much stronger than the Q_2 anomalies over WNP and are accompanied by larger PPE anomalies (Fig. 9d). Although the Q_1 and Q_2 anomalies both favor the enhancement of the PPE anomalies over SMC, only weakly positive PPE anomalies are evident there (Fig. 9d). These weakly positive PPE anomalies in the upper troposphere (600–300 hPa) over SMC may be caused by the opposing effects of the latent heat release and the surface heat fluxes (Fig. 7f). Overall, the Q_1 anomalies are the major contributor to the PPE anomalies in the upper troposphere (600–300 hPa) over WNP, and the Q_2 anomalies play the dominant role in controlling the lower troposphere (1000–700 hPa) PPE anomalies over SMC.

Equation (7) demonstrates that both the apparent heat source Q_1 and apparent moisture sink Q_2 can be divided into three terms: local changes ($c_p\partial T/\partial p$ and $-L\partial q/\partial t$), horizontal advections ($c_p\mathrm{V}\cdot\nabla T$ and $-L\mathrm{V}\cdot\nabla p$), and vertical transportations ($-c_p\omega\sigma$ and $-L\omega\partial q/\partial p$). As with Q_1 and Q_2, the vertical transportations ($-c_p\omega\sigma$ and $-L\omega\partial q/\partial p$) through the whole troposphere (1000–300 hPa) are still the major contributors to the PPE anomalies over the WNP and SMC when compared with the local changes ($c_p\partial T/\partial p$ and $-L\partial q/\partial p$) and horizontal advection ($c_p\mathrm{V}\cdot\nabla T$ and $-L\mathrm{V}\cdot\nabla q$; Fig. 10a and b). A similar situation can also be seen in the lower and upper troposphere (Fig. 10c and f). Compared with the lower troposphere (Fig. 10c), the vertical temperature transportation ($-c_p\omega\sigma$) anomalies in Q_1 are much larger (Fig. 10e). In

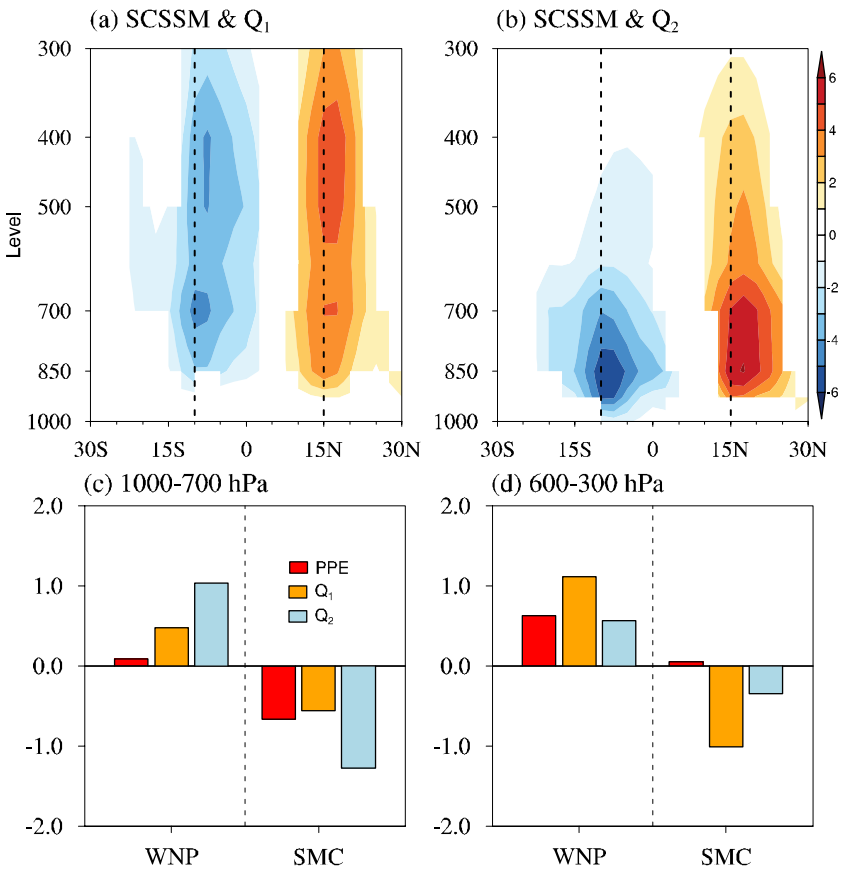

Fig. 9 Meridional-vertical **a** Q_1 (W m^{-2}) and **b** Q_2 anomalies (W m^{-2}) averaged between 100° E and 170° E regressed onto the SCSSMI during JJA. Area-averaged regression coefficients of the PPE (10^6 J m^{-2}), Q_1 and Q_2 ($\times 10^{-1}$ W m^{-2}) anomalies onto the SCSSMI over the WNP and SMC regions for the **c** lower (1000–700 hPa) and **d** upper (600–300 hPa) troposphere. Shading in **a** and **b** indicates that the values are significant at the 90% confidence level

contrast, the vertical moisture transportation ($-L\omega\partial q/\partial p$) anomalies in Q_2 are much stronger in the lower troposphere than in the upper troposphere (Figs. S10d–f). These results further demonstrate the important contributions of Q_1 (Q_2) to the PPE variations in the upper (lower) troposphere over the WNP and SMC.

6 Summary and discussion

Previous studies have investigated the dynamic processes associated with the SCSSM and their impact on IOD development using observational data and the CMIP5 models (Zhang et al. 2018, 2019b, 2021). Such circulation changes are essentially variations in energy; however, less attention has been paid to the energetic connection between the SCSSM and IOD. Therefore, this study investigated the energetic connection between the SCSSM and IOD based on the regional PPE theory on the interannual variability.

When the SCSSM is strong during JJA, the enhanced latent heating released by condensation related to precipitation increases the upper tropospheric PPE anomalies over the WNP, which corresponds to the negative C_k anomalies. This increased PPE is converted to PKE, and the anomalous ascending motion strengthens over the WNP. Correspondingly, the anomalous descending motion develops over the SMC through the regional Hadley circulation. This anomalous descending motion assists the decrease in the lower tropospheric PPE anomalies by reducing the specific humidity over the SMC, which corresponds to the positive C_k anomalies. The conversion of the PKE to PPE over the SMC further intensifies the local anomalous descending motion. The anomalous low-level southerly wind induced by the Coriolis force turns into the anomalous southeasterly wind off Sumatra and Java, further cooling the local SST anomalies through the WES and Bjerknes feedbacks (Zhang et al. 2018, 2021). With the increase in the zonal gradient of the SST anomalies over the tropical Indian Ocean, a positive IOD event intensifies during JJA, and vice versa. The increased zonal gradient of the PPE anomalies favors the Walker circulation over the tropical Indian Ocean during SON, further contributing to the maturation of the IOD. Therefore, the PPED over the WNP and SMC acts as a bridge that links the SCSSM to IOD, and a schematic

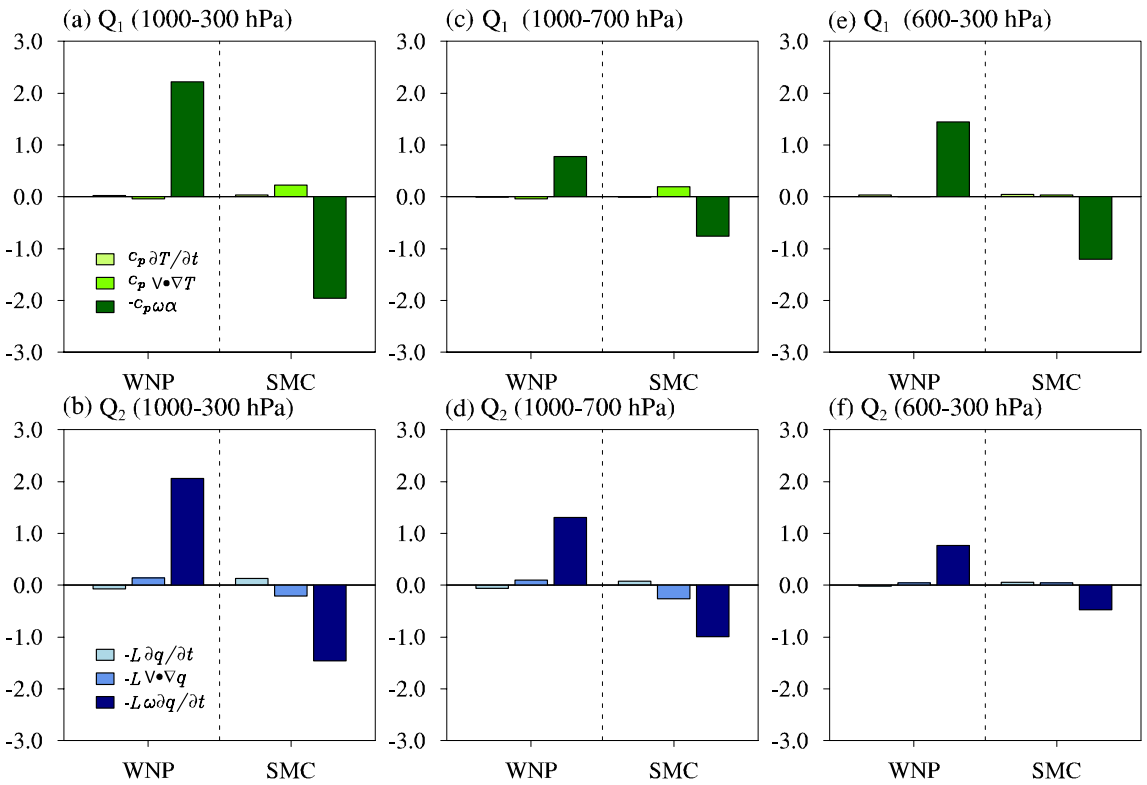

Fig. 10 The area-averaged regression coefficients of the local temperature change ($c_p\partial T/\partial p$, W m^{-2}, light green bars), the horizontal temperature advection ($c_p\mathrm{V}\cdot\nabla T$, W m^{-2}, green bars), and the vertical temperature transportation ($-c_p\omega\sigma$, $\times10^{-1}$ W m^{-2}, deep green bars) related to Q_1 on the SCSSMI in the **a** whole troposphere (1000–300 hPa), **b** lower troposphere (1000–700 hPa), and (**c**) upper troposphere (600–300 hPa) during JJA. **d–f**, as **a–c**, but for the local moisture change ($-L\partial q/\partial p$, W m^{-2}, light blue bars), the horizontal moisture advection ($-L\mathrm{V}\cdot\nabla q$, W m^{-2}, green bars), and the vertical moisture transportation ($-L\omega\partial q/\partial p$, $\times10^{-1}$ W m^{-2}, deep green bars) in Q_2

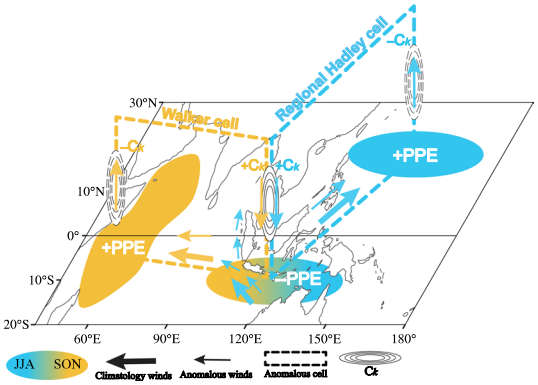

Fig. 11 Schematic representation of the energetic connection between the SCSSM and IOD. The + (−) symbols with the red (blue) shadings and solid (dashed) ellipse groups indicate the significant positive (negative) PPE and C_k anomalies for the strong SCSSM years. The blue and yellow colors denote the boreal JJA and SON, respectively. The gradients from blue to yellow present the PPE persisting from JJA to SON. Thick and thin vectors represent the mean climatology and anomalous wind. Dashed thick lines with vectors denote the regional Hadley (Walker) circulation over the WNP and SMC (tropical Indian Ocean)

representation of the associated mechanisms is shown in Fig. 11.

This study provides a new perspective to view the influence of the SCSSM on the IOD, deepening the understanding of the dynamic processes. Moreover, Zhang et al. (2019b) highlights the synergistic effects of the SCSSM and ENSO on the development of the IOD through the regional Hadley and Walker circulations, while the relevant energetic processes require deep investigation in the future. In addition, recent studies (Li et al. 2019; Yu et al. 2017, 2019) reported that the Asian summer monsoon experiences a prominent inter-decadal change, whether the inter-decadal change of the Asian summer monsoon can be well-captured in the atmospheric PPE variations is another interesting topic, which needs further detailed analyses.

Acknowledgements Thanks for the helpful suggestions from Dr. XG Yan. This work was jointly sponsored by the National Natural Science Foundation of China (NSFC) Project (42105055; 42130607), Shandong Natural Science Foundation Project (ZR2019ZD12), Qingdao Postdoctoral Applied Research Project (862105040041), Taishan Pandeng Scholar Project, the open fund of State Key Laboratory of Satellite Ocean Environment Dynamics, Second Institute of Oceanography, Ministry of Natural Resources (QNHX2217). Thanks for the Center for High Performance Computing and System Simulation, Laoshan Laboratory (Qingdao) for providing computing resource.

Author contributions YZ and JL contributed to the conceptualization and design of the study. Figures visualization and formal analysis were performed by YZ. YZ, JL, and YD analyzed and interpreted the energetic processes. The first draft of the manuscript was written by YZ, and all authors reviewed and approved the manuscript.

Funding This work was jointly sponsored by the National Natural Science Foundation of China (NSFC) Project (42105055; 42130607), Shandong Natural Science Foundation Project (ZR2019ZD12), Qingdao Postdoctoral Applied Research Project (862105040041), Taishan Pandeng Scholar Project, the open fund of State Key Laboratory of Satellite Ocean Environment Dynamics, Second Institute of Oceanography, Ministry of Natural Resources (QNHX2217).

Date availability NCEP/NCAR datasets were obtained from https://psl.noaa.gov/data/gridded/data.ncep.reanalysis.html; ERSST v5 downloaded at https://psl.noaa.gov/data/gridded/tables/sst.html; and SODA 2.2.4 was available at https://iridl.ldeo.columbia.edu/SOURCES/.CARTON-GIESE/.SODA/.v2p2p4/ssh/datafiles.html.

Declarations

Competing interests The authors declare no competing interests.

Conflict of interest I declare that the authors have no competing interests as defined by Springer, or other interests that might be perceived to influence the results and discussion reported in this paper.

References

Ashok K, Guan ZY, Yamagata T (2003) Influence of the Indian Ocean dipole on the Australian winter rainfall. Geophys Res Lett 30:1821. https://doi.org/10.1029/2003GL017926

Behera SK, Luo JJ, Masson S, Rao SA, Sakuma H, Yamagata T (2006) A CGCM study on the interaction between IOD and ENSO. J Clim 19:1688–1705. https://doi.org/10.1175/JCLI3797.1

Bretherton CS, Widmann M, Dymnidov VP, Wallace JM, Blade I (1999) The effective number of spatial degrees of freedom of a time-varying geld. J Clim 12:1990–2009. https://doi.org/10.1175/1520-0442(1999)0122.0.CO;2

Cai WJ, Cowan T, Sullivan A (2009) Recent unprecedented skewness towards positive Indian Ocean dipole occurrences and its impact on Australian rainfall. Geophys Res Lett 36:245–253. https://doi.org/10.1029/2009GL037604

Carton JA, Giese BS (2008) A reanalysis of ocean climate using Simple Ocean Data Assimilation (SODA). Mon Weather Rev 136:2999–3017. https://doi.org/10.1175/2007MWR1978.1

Chen JP, Yu JY, Wang X, Lian T (2020) Different influences of southeastern Indian Ocean and western Indian Ocean SST anomalies on eastern China rainfall during the decaying summer of 2015/16 extreme El Niño. J Clim 33:5247–5443. https://doi.org/10.1175/JCLI-D-19-0777.1

Ding RQ, Ha KJ, Li JP (2010) Interdecadal shift in the relationship between the East Asian summer monsoon and the tropical Indian Ocean. Clim Dyn 34:1059–1071. https://doi.org/10.1007/s00382-009-0555-2

Dong D, Li JP, Huyan LD, Xue JQ (2017) Atmospheric energetics over the tropical Pacific during the ENSO cycle. J Clim 30:3635–3654. https://doi.org/10.1175/JCLI-D-16-0480.1

Edmon HJ Jr (1978) A reexamination of limited-area available potential energy budget equations. J Atmos Sci 35:1655–1659. https://doi.org/10.1175/1520-0469(1978)035,1655:AROLAA.2.0.CO;2

Gao L, Li JP, Ren HL (2006) Some characteristics of the atmosphere during an adiabatic process. Prog Nat Sci 16:644–648. https://doi.org/10.1080/10020070612330047

Guan ZY, Yamagata T (2003) The unusual summer of 1994 in East Asia: IOD teleconnections. Geophys Res Lett 30:1544. https://doi.org/10.1029/2002GL016831

Hsu PC, Li T (2011) Interactions between boreal summer intraseasonal oscillations and synoptic-scale disturbances over the Western

North Pacific. Part II: apparent heat and moisture sources and eddy momentum transport. J Clim 24:942–961. https://doi.org/10.1175/2010JCLI3834.1

Huang BH, Shukla J (2007a) Mechanisms for the interannual variability in the tropical Indian Ocean. Part I: The role of remote forcing from the tropical Pacific. J Clim 20:2917–2936. https://doi.org/10.1175/JCLI4151.1

Huang BH, Shukla J (2007b) Mechanisms for the interannual variability in the tropical Indian Ocean. Part II: regional processes. J Clim 20:2937–2960. https://doi.org/10.1175/JCLI4169.1

Huang BY, Thorne PW, Banzon VF, Boyer T, Chepurin G, Lawrimore JH, Menne MJ, Smith TM, Vose RS, Zhang HM (2017) Extended reconstructed sea surface temperature, version 5 (ERSSTv5): upgrades, validations, and intercomparisons. J Clim 30:8179–8205. https://doi.org/10.1175/JCLI-D-16-0836.1

Huyan LD, Li JP, Zhao S, Sun C, Dong D, Liu T, Zhao YF (2017) The impact of layer perturbation potential energy on the East Asian summer monsoon. J Clim 30:7087–7103. https://doi.org/10.1175/JCLI-D-16-0729.1

Johnson DR (1970) The available potential energy of storms. J Atmos Sci 27:727–741. https://doi.org/10.1175/1520-0469(1970)027,0727:TAPEOS.2.0.CO;2

Kalnay E, Kanamitsu M, Kistler R, Collins W, Deaven D, Gandin L, Iredell M, Saha S, White G, Woollen J (1996) The NCEP/NCAR 40-year reanalysis project. Bull Am Meteorol Soc 77:437–471. https://doi.org/10.1175/1520-0477(1996)077%3c0437:TNYRP%3e2.0.CO;2

Kanno Y, Iwasaki T (2022) Future changes of atmospheric energy cycle in CMIP5 climate models. J Geophys Res: Atmos 127:e2021JD036380. https://doi.org/10.1029/2021JD036380

Kim YH, Kim MK (2013) Examination of the global Lorenz energy cycle using MERRA and NCEP-reanalysis 2. Clim Dyn 40:1499–1513. https://doi.org/10.1007/s00382-012-1358-4

Li JP, Gao L (2006) Theory on perturbation potential energy and its applications-concept, expression and spatio-temporal structures of perturbation potential energy (in Chinese). Chin J Geophys 30(5):834–848

Li JP, Zeng QC (2002) A unified monsoon index. Geophys Res Lett 29:1274. https://doi.org/10.1029/2001GL013874

Li JP, Zeng QC (2003) A new monsoon index and the geographical distribution of the global monsoons. Adv Atmosc Sci 20:299–302. https://doi.org/10.1007/s00376-003-0016-5

Li LM, Ingersoll AP, Jiang X, Feldman D, Yung YL (2007) Lorenz energy cycle of the global atmosphere based on reanalysis datasets. Geophys Res Lett 34:L16813. https://doi.org/10.1029/2007GL029985

Li JP, Wu ZW, Jiang ZH, He JH (2010) Can global warming strengthen the east Asian summer monsoon? J Clim 23:6696–6705. https://doi.org/10.1175/2010JCLI3434.1

Li LM, Jiang X, Chahine MT, Wang J, Yung YL (2011) The mechanical energies of the global atmosphere in El Niño and La Niña years. J Atmos Sci 68:3072–3078. https://doi.org/10.1175/JAS-D-11-072.1

Li JP, Sun C, Jin FF (2013) NAO implicated as a predictor of Northern Hemisphere mean temperature multidecadal variability. Geophys Res Lett 40:5497–5502. https://doi.org/10.1002/2013GL057877

Li JP, Zhao S, Li YJ, Wang L, Sun C (2016) On the role of perturbation potential energy in variability of the East Asian summer monsoon: Current status and prospects (in Chinese). Adv Earth Sci 31:115–125

Li J, Ding RQ, Wu ZW, Zhong QJ, Li BS, Li JP (2019) Inter-decadal change in potential predictability of the East Asian summer monsoon. Theor Appl Climatol 136:403–415. https://doi.org/10.1007/s00704-018-2482-9

Liu T, Li JP, Li YJ, Zhao S, Zheng F, Zheng JY, Yao ZX (2018) Influence of the May Southern annular mode on the South China Sea summer monsoon. Clim Dyn 51:4095–4107. https://doi.org/10.1007/s00382-017-3753-3

Lorenz EN (1955) Available potential energy and the maintenance of the general circulation. Tellus 7:157–167. https://doi.org/10.3402/tellusa.v7i2.8796

Margules M (1910) Uber die energie der stiirme (On the energy of storms). Zentralanstalt Meteor Geodyn 51:533–595

Nuncio M, Yuan X (2015) The influence of the Indian Ocean dipole on Antarctic sea ice. J Clim 28:2682–2690. https://doi.org/10.1175/JCLI-D-14-00390.1

Oort AH (1964) On estimates of the atmospheric energy cycle. Mon Weather Rev 92:483–499. https://doi.org/10.1175/1520-0493(1964)092,0483:OEOTAE.2.3.CO;2

Oort AH (1971) The observed annual cycle in the meridional transport of atmospheric energy. J Atmos Sci 28:325–339. https://doi.org/10.1175/1520-0469(1971)028,0325:TOACIT.2.0.CO;2

Oort AH, Ascher SC, Levitus S, Peixóto JP (1989) New estimates of the available potential energy in the world ocean. J Geophy Res 94:3187–3200. https://doi.org/10.1029/JC094iC03p03187

Pan Y, Li L, Jiang X, Li G, Zhang W, Wang X, Ingersoll AP (2017) Earth's changing global atmospheric energy cycle in response to climate change. Nat Commun 8:14367. https://doi.org/10.1038/ncomms14367

Peixóto JP, Oort AH (1974) The annual distribution of atmospheric energy on a planetary scale. J Geophys Res 79:2149–2159. https://doi.org/10.1029/JC079i015p02149

Roullet G, Capet X, Maze G (2014) Global interior eddy available potential energy diagnosed from Argo floats. Geophys Res Lett 41:1651–1656. https://doi.org/10.1002/2013GL059004

Saji NH, Yamagata T (2003) Structure of SST and surface wind variability during Indian Ocean dipole mode events: COADS observations. J Clim 16:2735–2751. https://doi.org/10.1175/1520-0442(2003)016,2735:SOSASW.2.0.CO;2

Saji NH, Goswami BN, Vinayachandran PN, Yamagata T (1999) A dipole mode in the tropical Indian Ocean. Nature 401:360–363. https://doi.org/10.1038/43854

Schott FA, Xie SP, McCreary JP Jr (2009) Indian Ocean circulation and climate variability. Rev Geophys 47:RG1002. https://doi.org/10.1029/2007RG000245

Sena AC, Magnusdottir G (2021) Influence of the Indian Ocean dipole on the large-scale circulation in South America. J Clim 34:6057–6068. https://doi.org/10.1175/JCLI-D-20-0669.1

Smith PJ (1969) On the contribution of a limited region to the global energy budget. Tellus 21:202–207. https://doi.org/10.1111/j.2153-3490.1969.tb00432.x

Smith PJ, Vincent DG, Edmon HJ Jr (1977) The time dependence of reference pressure in limited region available potential energy budget equations. Tellus 29:476–480. https://doi.org/10.1111/j.2153-3490.1977.tb00759.x

Stuecker MF, Timmermann A, Jin FF, Chikamoto Y, Zhang WJ, Wittenberg AT, Widiasih E, Zhao S (2017) Revisiting ENSO/Indian Ocean dipole phase relationships. Geophys Res Lett 44:2481–2492. https://doi.org/10.1002/2016GL072308

Wang B, Huang F, Wu Z, Yang J, Fu X, Kikuchi K (2009) Multi-scale climate variability of the South China Sea monsoon: a review. Dyn Atmos Oceans 47(1):15–37. https://doi.org/10.1016/j.dynatmoce.2008.09.004

Wang L, Li JP, Guo Y (2012) Governing equations of atmospheric layer perturbation potential energy and its applications—energy budget of the South China Sea summer monsoon activity (in Chinese). Chin J Atmos Sci 36:769–783

Wang YH, Li JP, Zhang YZ, Wang QY, Qin JH (2019) Atmospheric energetics over the tropical Indian Ocean during Indian Ocean dipole events. Clim Dyn 52:6243–6256. https://doi.org/10.1007/s00382-018-4510-y

Webster PJ, Moore AM, Loschnigg JP, Leben RR (1999) Coupled ocean–atmosphere dynamics in the Indian Ocean during 1997–98. Nature 401:356–360. https://doi.org/10.1038/43848

Xie SP, Annamalai H, Schott FA, McCreary JP Jr (2002) Structure and mechanisms of south Indian Ocean climate variability. J Clim 15:864–878. https://doi.org/10.1175/1520-0442(2002)015,0864:SAMOSI.2.0.CO;2

Yamagata T, Behera SK, Rao SA, Guan ZY, Ashok K, Saji HN (2003) Comments on '"Dipoles, temperature gradients, and tropical climate anomalies".' Bull Am Meteorol Soc 84:1418–1422. https://doi.org/10.1175/BAMS-84-10-1418

Yanai M, Tomita T (1998) Seasonal and interannual variability of atmospheric heat sources and moisture sinks as determined from NCEP–NCAR reanalysis. J Clim 11:463–482. https://doi.org/10.1175/1520-0442(1998)011%3c0463:SAIVOA%3e2.0.CO;2

Yang Y, Xie SP, Wu L, Kosaka Y, Lau N, Vecchi GA (2015) Seasonality and predictability of the Indian Ocean dipole mode: ENSO forcing and internal variability. J Clim 28:8021–8036. https://doi.org/10.1175/JCLI-D-15-0078.1

Yu L (2003) Variability of the depth of the 20°C isotherm along 68°N in the Bay of Bengal: Its response to remote and local forcing and its relation to satellite SSH variability. Deep-Sea Res Part II 50:2285–2304. https://doi.org/10.1016/S0967-0645(03)00057-2

Yu P, Zhang LF, Zhong QJ (2017) An interdecadal change in the relationship between the western North Pacific Ocean and the East Asian summer monsoon. Clim Dyn 49:1139–1156. https://doi.org/10.1007/s00382-016-3370-6

Yu P, Zhang LF, Zhong QJ (2019) Contrasting relationship between the Kuroshio Extension and the East Asian summer monsoon before and after the late 1980s. Clim Dyn 52:929–950. https://doi.org/10.1007/s00382-018-4173-8

Zhang WJ, Wang Y, Jin FF, Stuecker MF, Turner AG (2015) Impact of different El Niño types on the El Niño/IOD relationship. Geophys Res Lett 42:8570–8576. https://doi.org/10.1002/2015GL065703

Zhang YZ, Li JP, Xue JQ, Feng J, Wang QY, Xu YD, Wang YH, Zheng F (2018) Impact of the south China sea summer monsoon on the Indian Ocean dipole. J Clim 31:6557–6572. https://doi.org/10.1175/JCLI-D-17-0815.1

Zhang YZ, Li JP, Wang QY, Xue JQ (2019a) Variations in atmospheric perturbation potential energy associated with the South China Sea summer monsoon. Clim Dyn 53:2295–2308. https://doi.org/10.1007/s00382-019-04845-7

Zhang YZ, Li JP, Xue JQ, Zheng F, Wu RG, Ha KJ, Feng J (2019b) The relative roles of the South China Sea summer monsoon and ENSO in the Indian Ocean dipole development. Clim Dyn 53:6665–6680. https://doi.org/10.1007/s00382-019-04953-4

Zhang YZ, Li JP, Zheng F, Yu M, Feng J, Sun C (2021) Impact of the South China Sea summer monsoon on the Indian Ocean dipole in CMIP5 models. J Clim 34:1963–1981. https://doi.org/10.1175/JCLI-D-20-0582.1

Zhou ZQ, Xie SP, Zhang RH (2021) Historic Yangtze flooding of 2020 tied to extreme Indian Ocean conditions. Proc Natl Acad Sci 118:e2022255118. https://doi.org/10.1073/pnas.2022255118